Science Bulletin 64 (2019) 1617–1624

Contents lists available at ScienceDirect

Science Bulletin

journal homepage: www.elsevier.com/locate/scib

Science Bulletin
www.scibull.com

Article

Macroscopic synthesis of ultrafine N–doped carbon nanofibers for superior capacitive energy storage

Qiang Yu [a], Jianshuai Lv [a,b], Zhenhui Liu [a], Ming Xu [a], Wei Yang [a], Kwadwo Asare Owusu [a], Liqiang Mai [a], Dongyuan Zhao [a], Liang Zhou [a,*]

[a] State Key Laboratory of Advanced Technology for Materials Synthesis and Processing, Wuhan University of Technology, Wuhan 430070, China
[b] International School of Materials Science and Engineering, Wuhan University of Technology, Wuhan 430070, China

ARTICLE INFO

Article history:
Received 8 June 2019
Received in revised form 19 July 2019
Accepted 2 August 2019
Available online 9 August 2019

Keywords:
Macroscopic synthesis
Carbon
Nanofibers
N–doping
Supercapacitor

ABSTRACT

Carbon nanofibers (CNFs) with excellent electric conductivity and high surface area have attracted immense research interests in supercapacitors. However, the macroscopic production of CNFs still remains a great challenge. Herein, ultrafine N–doped CNFs (N–CNFs) with a diameter of ~20 nm are synthesized through a simple and scalable sol-gel method based on the self-assembly of phenolic resin and cetyltrimethylammonium bromide. When employed in aqueous supercapacitors, the obtained activated N–CNFs manifest a high gravimetric/areal capacitance (380 F g^{-1}/1.7 F cm^{-2}) as well as outstanding rate capability and cycling stability. Besides, the activated N–CNFs also demonstrate excellent capacitive performance (330 F g^{-1}) in flexible quasi-solid-state supercapacitors. The remarkable electrochemical performance as well as the easy and scalable synthesis makes the N–CNFs a highly promising electrode material for supercapacitors.

1. Introduction

Porous carbon materials have been extensively studied in supercapacitors owing to their high surface area and desirable conductivity [1]. Such carbon materials include graphene [2,3], carbon nanotubes [4–6], carbon nanofibers (CNFs) [7], spheres [8], nanosheets [9,10], microporous carbons [11], and mesoporous carbons [12,13]. Among the various carbon materials, CNFs with efficient one-dimensional (1D) electron-transport path along the axial direction and short ionic-diffusion distance along the radial direction are particularly attractive [14–16], which may serve as promising candidates for water treatment, electrocatalysis, and secondary batteries [17,18].

A number of methods have been developed towards the preparation of CNFs, including electrospinning [19,20], template-directed hydrothermal carbonization [21,22], direct pyrolysis of biomass (such as cellulose) [16], and chemical vapor deposition [23,24]. For example, Yu's group [7,25] developed a novel template-directed hydrothermal carbonization method for the mass production of CNFs using Te nanowires as the hard templates. No doubt, the above-mentioned approaches have achieved certain success in producing CNFs. However, they suffer from one or more of the following drawbacks, such as high cost, low yield, high energy consumption, employment of hazardous chemicals, and tedious synthesis procedure, which seriously hinder their scale-up production and practical applications. In this regard, a simple and environmental friendly approach for the macroscopic production of CNFs should be exploited.

Recently, Lu's group [26–28] developed a silica-assisted approach for the synthesis of CNFs based on the sol-gel chemistry of phenolic resin. However, the production of well-defined CNFs required the introduction of a silica coating layer and the removal of silica by HF after carbonization, which make the synthesis complex. Herein, we present a facile sol-gel synthesis approach towards the macroscopic production of ultrafine N–doped CNFs (designated as N–CNFs) with a uniform diameter of ~20 nm. The synthesis is simply based on the self-assembly of phenolic resin (3-aminophenol-formaldehyde) and cetyltrimethylammonium bromide (CTAB) in aqueous solution. N–CNFs with a high surface area of 1945 m^2 g^{-1} can be obtained after KOH activation. The abundant micropores provide numerous active sites for capacitive energy storage; the 1D nanofiber structure greatly accelerates the electron transfer; the ultrafine diameter significantly reduces the ion transport paths. When employed in supercapacitors, the activated N–CNFs manifest a high gravimetric/areal capacitance (380 F g^{-1}/1.7 F cm^{-2}) as well as outstanding rate and cycling performances in 6.0 mol L^{-1} KOH. In addition, the activated N–CNFs

* Corresponding author.
E-mail address: liangzhou@whut.edu.cn (L. Zhou).

https://doi.org/10.1016/j.scib.2019.08.008
2095-9273/

also demonstrate excellent capacitive performance (330 F g^{-1}) in flexible quasi-solid-state supercapacitors.

2. Experimental

2.1. Preparation of activated N–CNFs

In a typical synthesis, 0.2 g 3-aminophenol and 0.514 g hexamethylenetetramine (HMTA) were dissolved into 20 mL deionized water. Afterwards, 0.15 g CTAB was added and stirred for 20 min. The solution was heated to 85 °C and allowed to react under static condition for 24 h. The resulted resin/CTAB composite hydrogel was then freeze-dried. The as-synthesized dry aerogel was annealed at 800 °C for 5 h in N_2 to obtain the N–CNFs. The N–CNFs were activated by KOH at 700 °C for 2 h in N_2, and the KOH/N–CNFs mass ratio was 4. The activated N–CNFs were obtained after HCl (2.0 mol L^{-1}) treatment and drying. For comparison, activated N–doped carbon nanospheres (designated as N–CNSs) were also prepared by carbonization and activation of Resin-0.5 under the same conditions.

2.2. Fabrication of aqueous supercapacitors

The working electrode was prepared as follows: firstly, the activated N–CNFs and acetylene black with mass ratio of 80:10 were mixed; then, 10 wt% polytetrafluoroethylene (PTFE) was added to obtain a paste using an agate mortar and pestle. The electrode film was collected using a roller machine and dried at 80 °C. 6.0 mol L^{-1} KOH was used as the aqueous electrolyte. In three-electrode system, Pt plate was used as the counter electrode and saturated calomel electrode was used as the reference electrode.

2.3. Fabrication of flexible supercapacitors

The quasi-solid-state electrolyte was prepared as follows: 5.0 g polyvinyl alcohol (PVA) was dissolved in 50 mL water and stirred at 90 °C for 2 h. After dissolution, 10 mL 6.0 mol L^{-1} KOH solution was added dropwise. The PVA/KOH clear gel was solidified overnight for further use. The flexible symmetric supercapacitor was constructed with PVA/KOH gel as the electrolyte, polypropylene (NKK–MPF30AC) as the separator, and nickel foam as the current collector.

2.4. Materials characterization

Field-emission scanning electron microscopy (FESEM) images were carried out by a JEOL–7100F scanning electron microscope at 20 kV. Transmission electron microscopy (TEM), high-resolution TEM (HRTEM) images and energy dispersive X-ray spectra (EDS) elemental mappings were conducted on a JEM–2100F microscope at 200 kV. X-ray photoelectron spectroscopy (XPS) results were tested by a VG MultiLab 2000 instrument. Nitrogen adsorption–desorption isotherms were collected by Tristar-3020 and ASAP 2460 instruments at 77 K.

2.5. Electrochemical characterization

Cyclic voltammetry (CV), galvanostatic charge/discharge (GCD) and cycling stability tests were conducted with a CHI 760E instrument (Shanghai Chenhua Apparatus Co. Ltd.). The gravimetric specific capacitance C_g (F g^{-1}) in 3-electrode and symmetric 2-electrode systems were calculated from the discharge curve according to Eqs. (1) and (2), respectively:

$$C_g = \frac{I\Delta t}{m\Delta V}, \tag{1}$$

$$C_g = \frac{2I\Delta t}{m\Delta V}, \tag{2}$$

where I is the constant charge/discharge current, Δt is discharge time, ΔV is the working voltage window during the discharge process and m is the mass of active materials (single electrode).

The energy density (E_g, Wh kg^{-1}) and power density (P_g, W kg^{-1}) of aqueous and flexible quasi-solid-state symmetric supercapacitor devices were calculated using Eqs. (3) and (4), respectively:

$$E_g = \frac{C_g V^2}{2 \times 4}, \tag{3}$$

$$P_g = \frac{3600 E_g}{\Delta t}. \tag{4}$$

3. Results and discussion

The synthesis of the ultrafine N–CNFs is based on the sol-gel chemistry of phenolic resin and the self-assembly of phenolic resin and CTAB in aqueous solution, which is schematically illustrated in Fig. 1. During the sol-gel synthesis, 3-aminophenol and HMTA are employed as the precursors and CTAB is used as the structure-directing agent. At the reaction temperature of 85 °C, the HMTA hydrolyzes into formaldehyde and ammonia slowly. The in-situ generated formaldehyde then polymerizes with 3-aminophenol with the assistance of ammonia, generating a phenolic resin (3-aminophenol-formaldehyde) [29]. CTAB is a well-known cationic surfactant and its concentration in our work is 0.021 mol L^{-1}, which reaches its critical micelle concentration (CMC) for the formation of rod-like micelles. Under a basic condition, both the amino groups on phenolic resin and CTA^+ from the surfactant are positively charged. With the help of counter-ions (Br^-), the phenolic resin and CTAB rod-like micelles are self-assembled into composite mesostructured nanofibers through Coulombic forces (amino group$^+$∼Br^-∼CTA^+). After carbonization in N_2, the phenolic resin/CTAB composite nanofibers are converted into ultrafine N–CNFs. With subsequent activation by KOH, activated N–CNFs can be obtained.

The as-synthesized phenolic resin/CTAB composite shows a gel-like monolith morphology, which occupies the whole volume of the reactor. After removing the solvent by freeze-drying, aerogel monoliths can be obtained. Such monolith is relatively robust and possesses a very low density (0.02 g cm^{-3}), which can be held up by a Chinese rose (Fig. 2a inset). In addition, such composite aerogel monolith can be easily produced in large quantities. For example, ∼ 8.8 g of the resin/CTAB composite can be obtained in 400 mL of the solution, corresponding to a yield as high as 22 g L^{-1} (Fig. S1 online). Considering the facts that (1) the reactants, 3-aminophenol, HMTA, and CTAB, are relatively cheap and widely available and (2) the synthesis is conducted under mild conditions (85 °C) in aqueous solutions without any strong acids/bases, it is highly possible to realize large-scale production by simply employing larger reactors.

SEM images show that the as-prepared resin/CTAB composite is composed of ultrafine nanofibers with uniform diameters of ∼25 nm and lengths up to micrometers (Fig. 2a, b). The resin/CTAB nanofibers are interconnected with each other, forming a highly porous structure. After carbonization, the N–CNFs retain the original cross-linked nanofiber morphology (Figs. 2c and S2 (online)). Compared to the resin/CTAB composite, the N–CNFs present a reduced diameter of ∼20 nm, which is caused by the thermal induced shrinkage during carbonization. Even after further activation, the nanofiber structure can be well retained (Fig. 2d, e). HRTEM (Fig. 2f) reveals that the activated N–CNFs are generally

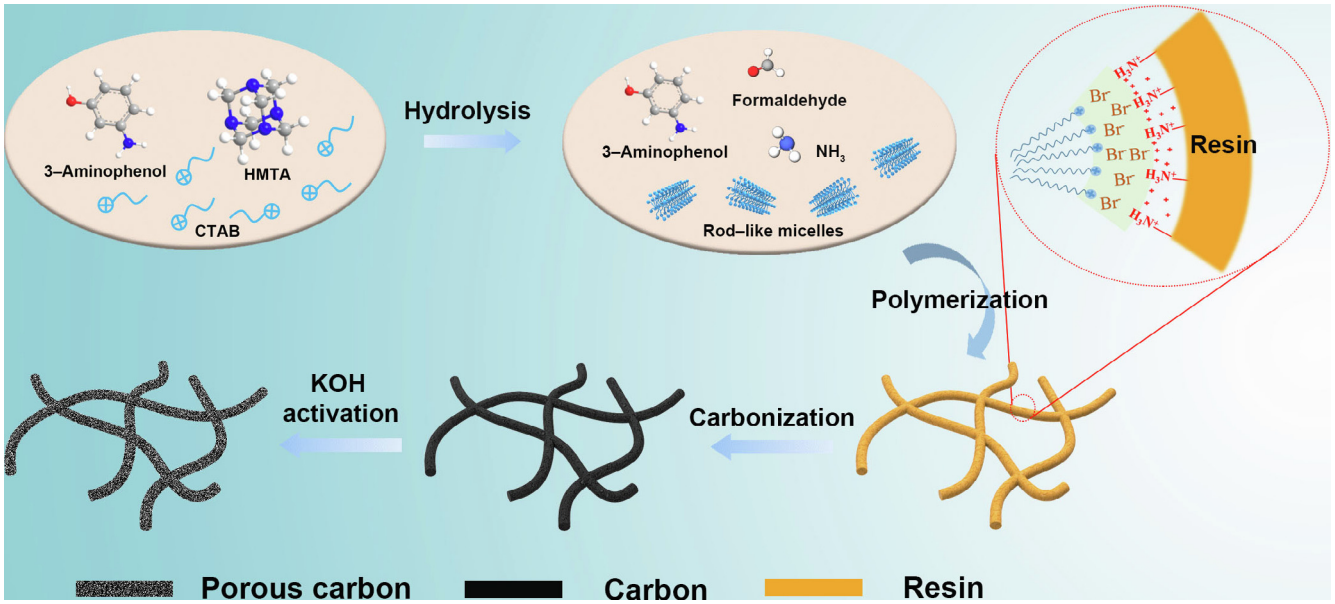

Fig. 1. (Color online) Schematic illustration for the fabrication of activated N–CNFs.

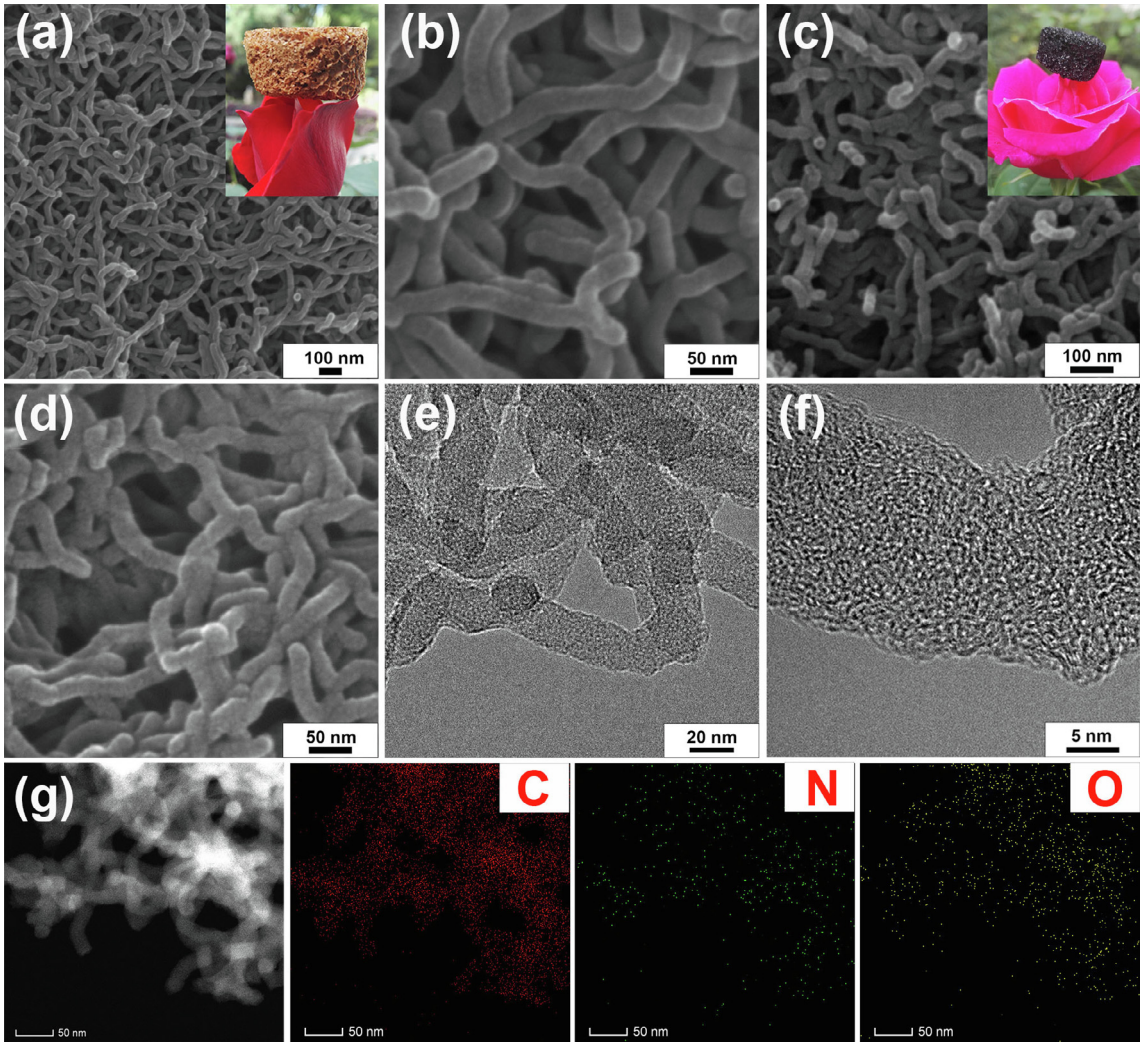

Fig. 2. (Color online) SEM images of resin/CTAB composite nanofibers (a, b), N–CNFs (c), and activated N–CNFs (d). TEM image (e), HRTEM image (f), and EDS elemental mapping (g) of the activated N–CNFs. The insets in (a) and (c) are digital photos of resin/CTAB composite and N–CNF based monoliths, respectively.

amorphous. EDS elemental mappings (Fig. 2g) demonstrate the homogeneous distribution of C, N, and O within the activated N–CNFs.

The X-ray diffraction (XRD) pattern of N–CNFs shows two broad diffraction peaks at ~24° and 43° (Fig. 3a), which is characteristic for amorphous carbon. After KOH activation, the diffraction peaks weaken and broaden, suggesting that the activation introduces more defects in the products. The possible reactions between KOH and carbon during the activation process may involve: $2\ KOH \rightarrow K_2O + H_2O$; $6\ KOH + 2\ C \rightarrow 2\ K + 3\ H_2 + 2\ K_2CO_3$; $K_2CO_3 \rightarrow CO_2 + K_2O$ [30]. Raman spectra of the N–CNFs and activated N–CNFs (Fig. 3b) feature a broad D-band at 1340 cm^{-1} and a relatively narrow G-band at 1590 cm^{-1} [31–33]. The D-band to G-band intensity ratio (I_D/I_G) of both samples are calculated to be around 1.0. To gain insights into the pore structure of the products, N_2 sorption measurements are carried out (Fig. 3c). The N–CNFs display a relatively low surface area of 96 $m^2\ g^{-1}$ and a pore volume of 0.28 $cm^3\ g^{-1}$ (Table S1 online). The activated N–CNFs manifest a typical type I isotherm, demonstrating its abundant microporous feature. The rich microporosity gives rise to a high surface area of 1945 $m^2\ g^{-1}$, among which 1768 $m^2\ g^{-1}$ is contributed from the micropores. In addition, the total pore volume and micropore volume of the activated N–CNFs are determined to be 1.49 and 0.90 $cm^3\ g^{-1}$, respectively. The pores are mainly distributed below 1 nm as can be observed from the pore size distribution (Fig. S3 online). The N_2 sorption results demonstrate that the KOH activation not only creates abundant micropores in the activated N–CNFs, but also introduces a certain amount of macropores, which can be reflected from the sharp increase in N_2 absorption amount at high relative pressure ($P/P_0 > 0.90$). When being applied in supercapacitors, both the micropores and macropores may play important roles in the electrochemical performance [34].

XPS is employed to study the surface element composition of the samples. Both samples are composed of C, N, and O (Fig. 3d). The N–CNFs have an N content of 4.95 at%. The KOH activation process etches part of the N atoms, leading to a decreased N content of 2.97 at% for activated N–CNFs. The N atoms at edge of the carbon rings are unstable, making them preferential regions for KOH etching at high temperatures [35]. Besides, the bulk N content of the activated N–CNFs is determined to be 3.15 at% by elemental analysis, which is consistent with the surface N content measured from XPS (2.97 at%). The high-resolution C1s spectrum (Fig. 3e) of activated N–CNFs displays three components: sp^2-bonded C at 284.6 eV, C—O and C—N at 285.9 eV, and C═O at 288.4 eV [36]. The N 1s core level spectrum (Fig. 3f) presents four peaks at 405.7, 401.4, 399.8, and 398.9 eV, corresponding to the pyridine N—O moieties, quaternary N, pyrrolic N, and pyridinic N, respectively [37]. The pyridinic and pyrrolic N, which are believed to be electrochemically active [38], account for 88% of total N in activated N–CNFs.

The polymerization of 3-aminophenol and HMTA (or formaldehyde) has been extensively studied in Refs. [12,29,39–41]. Usually, resin spheres have been obtained. In our study, uniform and ultrafine nanofibers are achieved. It is found that the HMTA/3–aminophenol molar ratio (x) plays an essential role in determining the morphology of resin (Table S2 online). With a low HMTA/3-aminophenol ratio ($x = 0.25$), the as-synthesized Resin-0.25 exhibits a uniform spherical morphology with a diameter of ~100 nm (Fig. S4a online). Increasing the HMTA/3-aminophenol ratio from 0.25 to 0.75 decreases the diameter of resin spheres from 100 to 70 nm (Figs. 3c, S4a (online)). This is because the polymerization is catalyzed by ammonia, which is in-situ generated by the hydrolysis of HMTA. With 3-aminophenol concentration unchanged, a higher HMTA/3-aminophenol ratio would lead to a higher ammonia concentration, which results in more resin nucleus and thus reduces particle size. Interestingly, when the HMTA/3-aminophenol ratio reaches 1.0, the resin spheres show a trend to merge with each other, forming dumbbell-shaped dimers (Fig. S4d online). With an even higher HMTA/3-aminophenol ratio ($x = 1.25$), ultrafine resin nanofibers dominate the sample with only a small fraction of resin spheres. Finally, when the HMTA/3-aminophenol ratio reaches 2.0, pure resin nanofibers can be obtained. It is speculated that such morphology evolution is originated from the variation in micelle shape. The self-assembly of

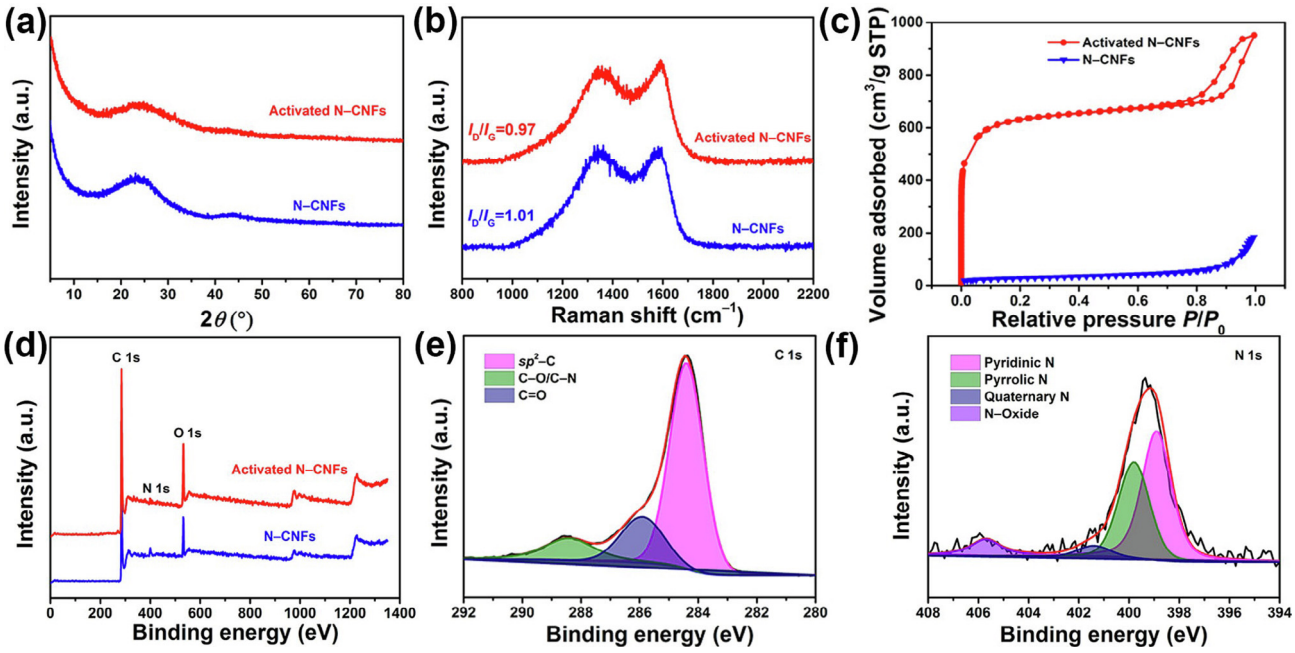

Fig. 3. (Color online) XRD patterns (a), Raman spectra (b), and N_2 adsorption/desorption isotherms (c) of N–CNFs and activated N–CNFs. XPS survey spectra (d) of N–CNFs and activated N–CNFs. High–resolution C1s (e) and N1s (f) spectra of the activated N–CNFs.

resin with spherical micelles through Coulombic forces leads resin/CTAB composite spheres, while the self-assembly of resin with rod-like micelles results in resin/CTAB composite nanofibers.

The effects of CTAB amount and reaction time on the morphology of resin/CTAB composites are further explored. Without CTAB, polydisperse resin spheres are obtained (Fig. S5a online). With the introduction of a small amount of CTAB (0.1 g), nanospheres are formed, and these nanospheres show an obvious tendency to merge into nanorods (Fig. S5b online). When the CTAB amount increases to 0.15 g or above, uniform resin/CTAB composite nanofibers are obtained (Figs. 4d, S5c (online)). It should be mentioned that 0.15 g CTAB corresponds to a concentration of 0.021 mol L^{-1}, which equals to the CMC of CTAB. To study the effects of reaction time, the HMTA/3-aminophenol molar ratio is fixed at 2.0 and the CTAB amount is fixed at 0.15 g. Resin/CTAB composite nanofibers can be formed within 3 h and the length of nanofibers increases with the reaction time in general (Fig. S6 online).

The large specific surface area, hierarchical porosity, and ultrafine diameter render the activated N–CNFs an ideal candidate material for supercapacitors. Fig. 4 presents supercapacitor performance of the activated N–CNFs in 6.0 mol L^{-1} KOH. The CV curves of the activated N–CNFs exhibit a two-fold current response to that of N–CNF, suggesting its enhanced capacitance (Fig. 4a). Even at 100 mV s^{-1}, the activated N–CNFs display a quasi-rectangular shaped CV curve (Fig. 4b), demonstrating the ideal capacitive charge storage mechanism. Besides, the activated N–CNFs display equilateral triangular shaped GCD profiles at 1–20 A g^{-1} (Fig. 4c). Even at 20 A g^{-1}, the activated N–CNFs show negligible IR drop in GCD curves, indicating its high electrical conductivity. The activated N–CNFs deliver a gravimetric capacitance of 380 F g^{-1} at 1 A g^{-1}. Considering the mass loading of activated N–CNFs in the electrode (2.39 mg cm^{-2}), the areal capacitance reaches 908 mF cm^{-2}. Even at 100 A g^{-1}, a superior capacitance of 226 F g^{-1} can be achieved. For comparison, the N–CNFs deliver a much lower capacitance of 141 F g^{-1} at 1 A g^{-1} (Fig. 4d). Usually, the supercapacitor performance is highly dependent on the mass loading. Considering this fact, the mass loading of activated N–CNFs is varied from 2.4 to 5.6 mg cm^{-2}. As for the activated N–CNFs, high gravimetric and areal capacitances (304 F g^{-1} and 1.7 F cm^{-2}) can be obtained at a high mass loading of ~5.6 mg cm^{-2} (Figs. 4e, S7 (online)). Furthermore, the activated N–CNFs also demonstrate outstanding cycling stability with negligible capacitance fading after 10,000 cycles at 20 A g^{-1} (Fig. 4f).

The supercapacitor performances of activated N–CNFs prepared at different activation temperatures are also investigated. Among the activated N–CNFs prepared at 600, 700, and 800 °C, the sample activated at 700 °C demonstrates the highest specific capacitance (Fig. S8 online). The sample prepared at 800 °C delivers much lower specific capacitance due to the overactivation and structural damage at high temperature. The capacitive performances of N–CNSs are also evaluated for comparison. The specific capacitance (359 F g^{-1}) and rate performance of activated N–CNSs are not as good as those of the activated N–CNFs (Fig. S9 online) owing to the aggregation of nanospheres.

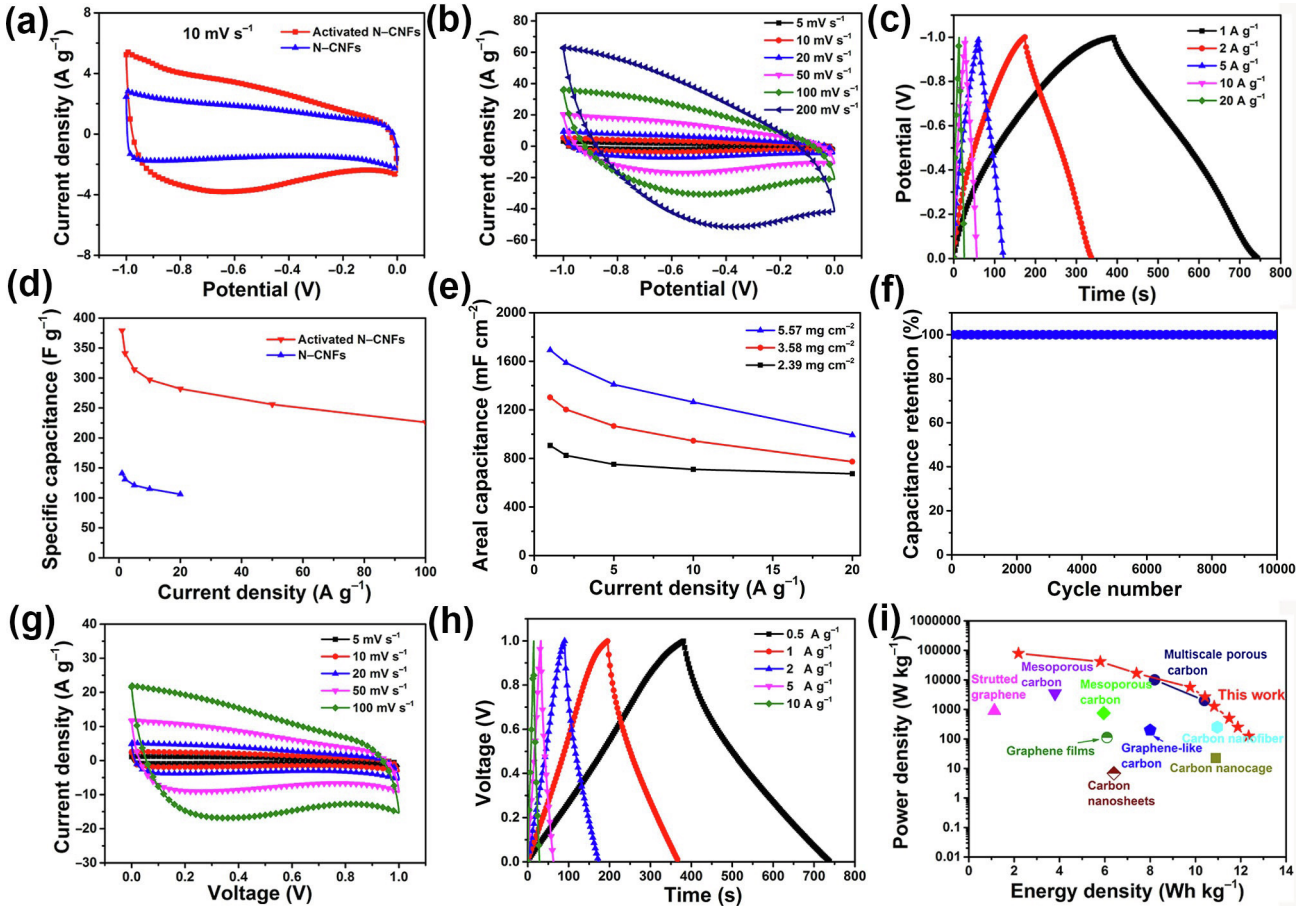

Fig. 4. (Color online) Supercapacitor performances of N–CNFs and activated N–CNFs in 6.0 mol L^{-1} KOH. Three-electrode system: CV profiles at 10 mV s^{-1} (a); CV profiles of activated N–CNFs at various sweep rates (b); GCD curves of activated N–CNFs at various current densities (c); rate performances of activated N–CNFs and N–CNFs (d); rate performances of activated N–CNFs at different mass loadings (e); cycling stability of activated N–CNFs at 20 A g^{-1} (f). Two-electrode system: CV curves of activated N–CNFs at various sweep rates (g); GCD curves of activated N–CNFs at various current densities (h); Ragone plots showing the power density vs. energy density (i).

The supercapacitor performances of activated N–CNFs in two-electrode symmetric cells are also investigated. Just like in three-electrode configuration, the N–CNFs based symmetric cell display rectangular shaped CV curves (Figs. 4g, S10a (online)) and isosceles triangular shaped GCD profiles (Figs. 4h, S10b (online)), demonstrating the outstanding capacitive behavior. The specific capacitances of the activated N–CNFs at 0.5, 1, 2, 5, and 10 A g^{-1} are calculated to be 356, 342, 331, 313, and 300 F g^{-1} (Fig. 4h), respectively. Even at 100 A g^{-1}, the activated N–CNFs show a small IR drop in GCD profile and deliver a capacitance of 167 F g^{-1} (Fig. S11 online), demonstrating the excellent rate performance. Besides the high capacitance and ideal rate capability, the activated N–CNFs based symmetric cell also presents desirable cyclability with 95.1% capacitance retention for 10,000 cycles (Fig. S12 online). From electrochemical impedance spectroscopy (EIS) test, the intrinsic ohmic resistance (R_s) and charge transfer resistance (R_{ct}) of the activated N–CNFs are calculated to be only 0.8 and 1.72 Ω, respectively (Fig. S13 online), demonstrating the good electrode conductivity and electron transfer efficiency. Based on the mass of active materials, the symmetric cell exhibits a maximum energy density of 12.35 Wh kg^{-1} at 130 W kg^{-1} (Fig. 4i). The maximum power density can reach as high as 78.75 kW kg^{-1}. The energy and power densities of the activated N–CNFs based symmetric cell are compared with other porous carbon based aqueous supercapacitors in the Ragone plot. The activated N–CNFs demonstrate more comparable or even superior supercapacitor performance than other state-of-the-art porous carbon materials (Table S3 online) [20,42–49]. To further enhance the energy density of the activated N–CNFs based supercapacitors, the aqueous electrolyte (6.0 mol L^{-1} KOH) is replaced by commercial organic electrolyte (TEABF$_4$/AN). The employment of organic electrolyte extends the voltage window of symmetric cells to 2.7 V. The activated N–CNFs deliver a capacitance of 143 F g^{-1} at 0.5 A g^{-1} in TEABF$_4$/AN (Fig. S14 online).

To evaluate the potential of activated N–CNFs for flexible electronics, flexible quasi-solid-state symmetric supercapacitors are also assembled (Fig. 5a, b). As in aqueous electrolytes, the as-assembled flexible supercapacitor exhibits quasi-rectangular CV curves (Fig. 5c). Due to the high viscosity of gel electrolyte, the ion diffusion rate is not comparable to that in aqueous electrolytes. As a result, the rate performance of quasi-solid-state supercapacitor is not as good as that of the aqueous supercapacitors. The capacitances determined from GCD curves are 330 and 172 F g^{-1} at 0.5 and 20 A g^{-1}, respectively (Fig. 5d). It is worth noting that there is no significant IR drop, even at high current density, which further confirms the excellent electrode conductivity. Interestingly, the as-fabricated quasi-solid-state supercapacitor can be bent with large angles without sacrificing the electrochemical performance (Fig. 5e), testifying the excellent flexibility of the device. The maximum energy and power densities of quasi-solid-state supercapacitor reach 11.04 Wh kg^{-1} and 12.50 kW kg^{-1} (Fig. 5f), respectively. Such values are comparable to those of the flexible quasi-solid-state supercapacitors reported recently [50–52]. By connecting three flexible supercapacitors in series, 42 and 60 LEDs can be lit up for 2 min (Movie S1 and Fig. S15 online), manifesting a great potential in energy storage.

In general, the activated N–CNFs demonstrate excellent gravimetric/areal capacitance and rate capability. The high capacitance can be ascribed to the rich microporosity which provides numerous active sites for capacitive energy storage. The superior rate performance is associated with ultrafine N–doped nanofibrous structure. In detail, the activated N–CNFs with ultrafine diameter (~20 nm) provide significantly reduced ion transport distance. The interconnected nanofibers provide a continuous pathway for electron transport. Besides, the rich N functionalities improve the electrolyte wettability (Fig. S16 online) and the inter-fiber macropores assure the easy penetration of electrolyte ions. These features together render the activated N–CNFs an ideal electrode material for supercapacitors.

4. Conclusion

In conclusion, ultrafine N–doped carbon nanofibers (N–CNFs) with a uniform diameter of ~20 nm are successfully produced

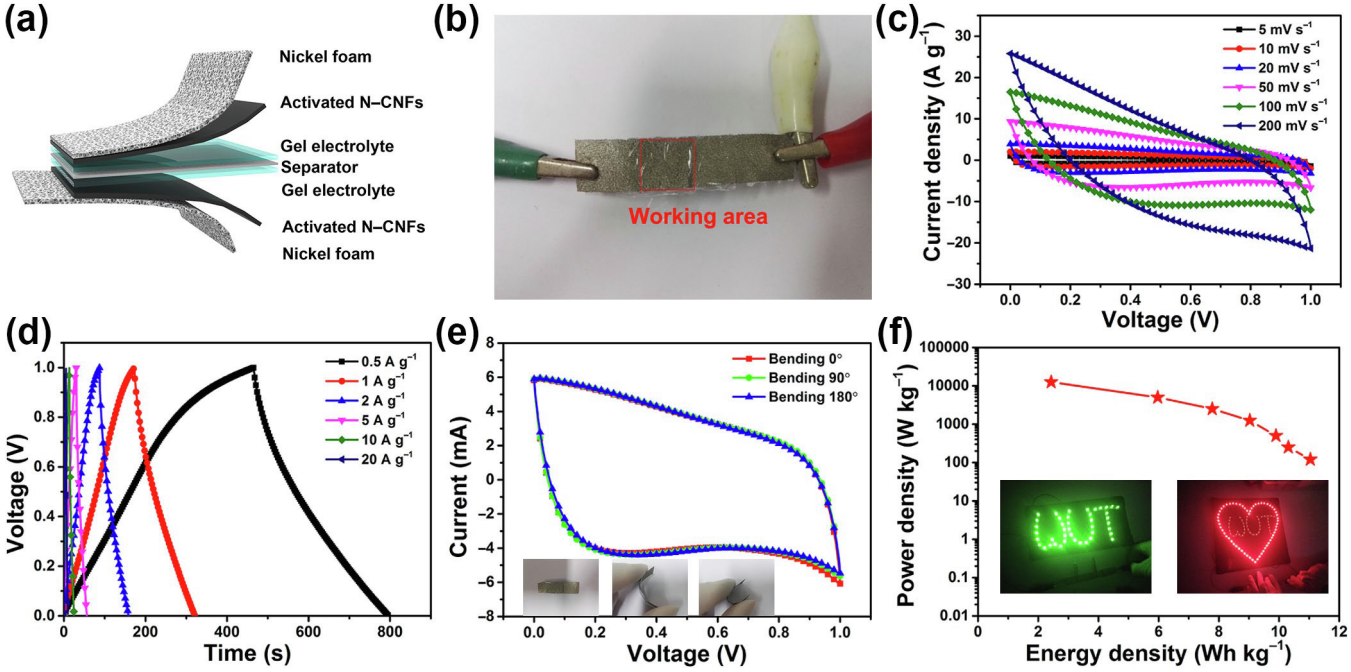

Fig. 5. (Color online) Flexible supercapacitor performances: schematic illustration (a) and digital image (b) of a flexible quasi-solid-state symmetric supercapacitor device; CV curves at various sweep rates (c); GCD curves at various current densities (d); flexibility test (e); Ragone plot showing the power density vs. energy density of the activated N–CNFs based flexible quasi-solid-state supercapacitor (f).

macroscopically through a sol-gel method based on the self-assembly of phenolic resin and cetyltrimethylammonium bromide. The abundant micropores, rich N–doping, and ultrafine 1D nanofibrous structure endow the activated N–CNFs excellent capacitive performance. The activated N–CNFs manifest a high gravimetric/areal capacitance (380 F g^{-1}/1.7 F cm^{-2}) as well as outstanding rate and cycling performances in 6.0 mol L^{-1} KOH. The activated N–CNFs also demonstrate excellent capacitive performance (330 F g^{-1}) in flexible quasi-solid-state supercapacitors. This work provides a new paradigm for the macroscopic production of ultrafine N–CNFs with ideal capacitive performance for supercapacitors. It is anticipated that the ultrafine N–CNFs may also serve as a promising candidate for water treatment, electrocatalysis, and secondary batteries.

Conflict of interest

The authors declare that they have no conflict of interest.

Acknowledgments

This work was supported by the National Key Research and Development Program of China (2016YFA0202603), the National Natural Science Foundation of China (21673171), the Program of Introducing Talents of Discipline to Universities (B17034), and the National Natural Science Fund for Distinguished Young Scholars (51425204).

Author contributions

Qiang Yu and Jianshuai Lv carried out the experiment. Qiang Yu, Zhenhui Liu and Ming Xu conducted the materials characterization. Wei Yang designed and conducted the 3D schematic illustration. Qiang Yu and Kwadwo Asare Owusu performed the electrochemical test and analyses. Liqiang Mai and Dongyuan Zhao provided the guidance for the whole research process and revised the paper. Liang Zhou designed the research and wrote the paper with Qiang Yu. All authors discussed the results and commented on the manuscript.

Appendix A. Supplementary data

Supplementary data to this article can be found online at https://doi.org/10.1016/j.scib.2019.08.008.

References

[1] Zhai YP, Dou YQ, Zhao DY, et al. Carbon materials for chemical capacitive energy storage. Adv Mater 2011;23:4828–50.
[2] Zhu YW, Murali S, Stoller M, et al. Carbon-based supercapacitors produced by activation of graphene. Science 2011;332:1537.
[3] Yang XW, Cheng C, Wang YF, et al. Liquid-mediated dense integration of graphene materials for compact capacitive energy storage. Science 2013;341:534–7.
[4] Yu D, Goh K, Wang H, et al. Scalable synthesis of hierarchically structured carbon nanotube-graphene fibres for capacitive energy storage. Nat Nanotechnol 2014;9:555.
[5] Fan ZJ, Yan J, Zhi LJ, et al. Three-dimensional carbon nanotube/graphene sandwich and its application as electrode in supercapacitors. Adv Mater 2010;22:3723–8.
[6] Tan B, Wu ZF, Xie ZL. Fine decoration of carbon nanotubes with metal organic frameworks for enhanced performance in supercapacitance and oxygen reduction reaction. Sci Bull 2017;62:1132–41.
[7] Chen LF, Feng Y, Liang HW, et al. Macroscopic-scale three-dimensional carbon nanofiber architectures for electrochemical energy storage devices. Adv Energy Mater 2017;7:1700826.
[8] Xu M, Yu Q, Liu ZH, et al. Tailoring porous carbon spheres for supercapacitors. Nanoscale 2018;10:21604–16.
[9] Jin ZY, Lu AH, Xu YY, et al. Ionic liquid-assisted synthesis of microporous carbon nanosheets for use in high rate and long cycle life supercapacitors. Adv Mater 2014;26:3700–5.
[10] Zheng X, Luo J, Lv W, et al. Two-dimensional porous carbon: synthesis and ion-transport properties. Adv Mater 2015;27:5388–95.
[11] Chmiola J, Yushin G, Gogotsi Y, et al. Anomalous increase in carbon capacitance at pore sizes less than 1 nanometer. Science 2006;313:1760–3.
[12] Shen GZ, Sun XR, Zhang HW, et al. Nitrogen-doped ordered mesoporous carbon single crystals: aqueous organic-organic self-assembly and superior supercapacitor performance. J Mater Chem A 2015;3:24041–8.
[13] Wang DW, Li F, Chen ZG, et al. Synthesis and electrochemical property of boron-doped mesoporous carbon in supercapacitor. Chem Mater 2008;20:7195–200.
[14] Chen LF, Zhang XD, Liang HW, et al. Synthesis of nitrogen-doped porous carbon nanofibers as an efficient electrode material for supercapacitors. ACS Nano 2012;6:7092–102.
[15] Chen LF, Huang ZH, Liang HW, et al. Flexible all-solid-state high-power supercapacitor fabricated with nitrogen-doped carbon nanofiber electrode material derived from bacterial cellulose. Energy Environ Sci 2013;6:3331–8.
[16] Chen LF, Huang ZH, Liang HW, et al. Three-dimensional heteroatom-doped carbon nanofiber networks derived from bacterial cellulose for supercapacitors. Adv Funct Mater 2014;24:5104–11.
[17] Wang AX, Zhang XY, Yang YW, et al. Horizontal centripetal plating in the patterned voids of Li/graphene composites for stable lithium-metal anodes. Chem 2018;4:2192–200.
[18] Liu S, Wang AX, Li QQ, et al. Crumpled graphene balls stabilized dendrite-free lithium metal anodes. Joule 2018;2:184–93.
[19] Tan J, Han YL, He L, et al. In situ nitrogen-doped mesoporous carbon nanofibers as flexible freestanding electrodes for high-performance supercapacitors. J Mater Chem A 2017;5:23620–7.
[20] Chen LF, Lu Y, Yu L, et al. Designed formation of hollow particle-based nitrogen-doped carbon nanofibers for high-performance supercapacitors. Energy Environ Sci 2017;10:1777–83.
[21] Liang HW, Guan QF, Chen LF, et al. Macroscopic-scale template synthesis of robust carbonaceous nanofiber hydrogels and aerogels and their applications. Angew Chem Int Ed 2012;51:5101–5.
[22] Song LT, Wu ZY, Liang HW, et al. Macroscopic-scale synthesis of nitrogen-doped carbon nanofiber aerogels by template-directed hydrothermal carbonization of nitrogen-containing carbohydrates. Nano Energy 2016;19:117–27.
[23] Liu YF, Luo JJ, Helleu C, et al. Hierarchical porous carbon fibers/carbon nanofibers monolith from electrospinning/CVD processes as a high effective surface area support platform. J Mater Chem A 2017;5:2151–62.
[24] Wang Q, Zhou ZY, Lai YZ, et al. Phenylenediamine-based FeN_x/c catalyst with high activity for oxygen reduction in acid medium and its active-site probing. J Am Chem Soc 2014;136:10882–5.
[25] Zhang W, Wu ZY, Jiang HL, et al. Nanowire-directed templating synthesis of metal-organic framework nanofibers and their derived porous doped carbon nanofibers for enhanced electrocatalysis. J Am Chem Soc 2014;136:14385–8.
[26] Sun Q, Zhang XQ, Han F, et al. Controlled hydrothermal synthesis of 1D nanocarbons by surfactant-templated assembly for use as anodes for rechargeable lithium-ion batteries. J Mater Chem 2012;22:17049–54.
[27] Zhang XQ, Sun Q, Dong W, et al. Synthesis of superior carbon nanofibers with large aspect ratio and tunable porosity for electrochemical energy storage. J Mater Chem A 2013;1:9449.
[28] Zhang XQ, He B, Li WC, et al. Hollow carbon nanofibers with dynamic adjustable pore sizes and closed ends as hosts for high-rate lithium-sulfur battery cathodes. Nano Res 2018;11:1238–46.
[29] Yu Q, Guan DD, Zhuang ZC, et al. Mass production of monodisperse carbon microspheres with size-dependent supercapacitor performance via aqueous self-catalyzed polymerization. ChemPlusChem 2017;82:872.
[30] Wu TJ, Jing MJ, Tian Y, et al. Surface-driven energy storage behavior of dual-heteroatoms functionalized carbon material. Adv Funct Mater 2019;29:1900941.
[31] Cui XQ, Pan ZY, Zhang LJ, et al. Selective etching of nitrogen-doped carbon by steam for enhanced electrochemical CO_2 reduction. Adv Energy Mater 2017;7:1701456.
[32] Feng LX, Wang K, Zhang X, et al. Flexible solid-state supercapacitors with enhanced performance from hierarchically graphene nanocomposite electrodes and ionic liquid incorporated gel polymer electrolyte. Adv Funct Mater 2018;28:1704463.
[33] Li C, Zhang X, Wang K, et al. Scalable self-propagating high-temperature synthesis of graphene for supercapacitors with superior power density and cyclic stability. Adv Mater 2017;29:1604690.
[34] Wang DW, Li F, Liu M, et al. 3D aperiodic hierarchical porous graphitic carbon material for high-rate electrochemical capacitive energy storage. Angew Chem Int Ed 2008;47:373–6.
[35] Yao L, Wu Q, Zhang PX, et al. Scalable 2D hierarchical porous carbon nanosheets for flexible supercapacitors with ultrahigh energy density. Adv Mater 2018;30:1706054.
[36] Wang J, Liu HY, Diao JY, et al. Size-controlled nitrogen-containing mesoporous carbon nanospheres by one-step aqueous self-assembly strategy. J Mater Chem A 2015;3:2305–13.
[37] Wickramaratne NP, Xu JT, Wang M, et al. Nitrogen enriched porous carbon spheres: attractive materials for supercapacitor electrodes and CO_2 adsorption. Chem Mater 2014;26:2820–8.
[38] Gao XY, Li XY, Kong Z, et al. Bifunctional 3D N–doped porous carbon materials derived from paper towel for oxygen reduction reaction and supercapacitor. Sci Bull 2018;63:621–8.

[39] Zhao JM, Niu WX, Zhang L, et al. A template-free and surfactant-free method for high-yield synthesis of highly monodisperse 3-aminophenol-formaldehyde resin and carbon nano/microspheres. Macromolecules 2012;46:140–5.
[40] Liu J, Yang TY, Wang DW, et al. A facile soft-template synthesis of mesoporous polymeric and carbonaceous nanospheres. Nat Commun 2013;4:2798.
[41] Feng SH, Liu ZH, Yu Q, et al. Monodisperse carbon sphere-constructed pomegranate-like structures for high-volumetric-capacitance supercapacitors. ACS Appl Mater Interfaces 2019;11:4011–6.
[42] Wang XB, Zhang YJ, Zhi CY, et al. Three-dimensional strutted graphene grown by substrate-free sugar blowing for high-power-density supercapacitors. Nat Commun 2013;4:2905.
[43] Liu RL, Wan L, Liu SQ, et al. An interface-induced co-assembly approach towards ordered mesoporous carbon/graphene aerogel for high-performance supercapacitors. Adv Funct Mater 2015;25:526–33.
[44] He XJ, Li RC, Qiu JS, et al. Synthesis of mesoporous carbons for supercapacitors from coal tar pitch by coupling microwave-assisted KOH activation with a MgO template. Carbon 2012;50:4911–21.
[45] Zhang F, Liu TY, Li MY, et al. Multiscale pore network boosts capacitance of carbon electrodes for ultrafast charging. Nano Lett 2017;17:3097–104.
[46] Zhao J, Jiang YF, Fan H, et al. Porous 3D few-layer graphene-like carbon for ultrahigh-power supercapacitors with well-defined structure-performance relationship. Adv Mater 2017;29:1604569.
[47] Zhao J, Lai HW, Lyu ZY, et al. Hydrophilic hierarchical nitrogen-doped carbon nanocages for ultrahigh supercapacitive performance. Adv Mater 2015;27:3541–5.
[48] Bo Z, Zhu WG, Ma W, et al. Vertically oriented graphene bridging active-layer/current-collector interface for ultrahigh rate supercapacitors. Adv Mater 2013;25:5799–806.
[49] Fan XM, Yu C, Yang J, et al. A layered-nanospace-confinement strategy for the synthesis of two-dimensional porous carbon nanosheets for high-rate performance supercapacitors. Adv Energy Mater 2015;5:1401761.
[50] Jiang DG, Li CW, Yang WR, et al. Fabrication of an arbitrary-shaped and nitrogen-doped graphene aerogel for highly compressible all solid-state supercapacitors. J Mater Chem A 2017;5:18684–90.
[51] Kai Q, Hou RZ, Zaman S, et al. A core/shell structured tubular graphene nanoflake-coated polypyrrole hybrid for all-solid-state flexible supercapacitors. J Mater Chem A 2018;6:3913–8.
[52] Li Z, Huang TQ, Gao WW, et al. Hydrothermally activated graphene fiber fabrics for textile electrodes of supercapacitors. ACS Nano 2017;11:11056–65.

Qiang Yu is now a Ph.D. candidate at Wuhan University of Technology with Profs. Liqiang Mai and Dongyuan Zhao. His research interests focus on the development of nanostructured carbon nanomaterials for supercapacitors and lithium-ion batteries.

Liang Zhou received his Ph.D. (2011) degree from Department of Chemistry, Fudan University. After graduation, he worked as a postdoctoral research fellow at Nanyang Technological University (2011–2012) and The University of Queensland (2012–2015). He is now a full professor at Wuhan University of Technology. His research interests include functional nanomaterials for electrochemical energy storage.